The mass dependence of halo alignments with large-scale structure

Davide Piras[1]* and more

[1]*Dipartimento di Fisica "G. Galilei", Università di Padova, via Marzolo 8, I-35131 Padova, Italy*

5 May 2017

ABSTRACT

This is a simple template for authors to write new MNRAS papers. The abstract should briefly describe the aims, methods, and main results of the paper. It should be a single paragraph not more than 250 words (200 words for Letters). No references should appear in the abstract.

Key words: galaxies: halos – dark matter – large-scale structure of universe

1 INTRODUCTION

When looking at the sky, assuming a homogeneous and isotropic universe, one would expect to see randomly distributed galaxies with arbitrary orientation, whereas correlation between galaxy shapes is actually observed. Plenty of reasons can be exhibited to explain this, such as the effect of gravitational tidal fields from the surrounding dark matter haloes and the accretion of new material along favoured directions: this phenomenon is known as intrinsic alignment (sometimes referred to as IA; see Troxel & Ishak (2015); Joachimi et al. (2015); Kiessling et al. (2015) for recent reviews). Besides carrying information about galaxy formation, IA contributes to the overall cosmic shear signal: Heavens et al. (2000) and Croft & Metzler (2000) first showed the non-negligible contamination of the weak lensing signal due to correlations in the intrinsic shapes of galaxies using simulated data, and many other works afterwards (Heymans et al. (2006); Semboloni et al. (2008), just to mention two of them) confirmed that this effect must be taken into consideration in order not to bias the results from deep lensing surveys, such as LSST (LSST Science Collaboration et al. 2009) and Euclid (Laureijs et al. 2011).

Measurements of the intrinsic alignment signal have been performed using data from hydrodynamical simulations (Codis et al. 2015; Velliscig et al. 2015; Chisari et al. 2015; Hilbert et al. 2017; Tenneti et al. 2016), from N-body simulations (Heavens et al. 2000; Croft & Metzler 2000; Jing 2002; Kuhlen et al. 2007; Schneider et al. 2012), as already mentioned, and considering observation data as well (Mandelbaum et al. 2006; Hirata et al. 2007; Okumura et al. 2009; Hao et al. 2011; van Uitert & Joachimi 2017), claiming that massive red galaxies point towards matter overdensities, while blue galaxies do not show any clear hint of alignment (Hirata et al. 2007; Mandelbaum et al. 2011).

The dependence of the IA signal with redshift and mass has also been studied: Hao et al. (2011), for example, studied a large sample of galaxy clusters from the SDSS DR7 finding a strong dependence of the alignment with redshift and an increasing trend with the mass of the brightest cluster galaxy. Moreover, Jing (2002) used a 512^3-particle simulation to get accurate formulae to fit the ellipticity correlation function over three orders of magnitude in mass, while an increasing trend of the IA amplitude with luminosity, or the corresponding mass, has been identified using real data, for galaxies (Joachimi et al. 2011; Singh et al. 2015) and for clusters (van Uitert & Joachimi 2017). In order to assume more stringent priors on the parameters of the models that will be adopted by future surveys, it is important to obtain accurate constraints on these dependences.

In this work, we delve into the dependence of the amplitude of the intrinsic alignment signal on the mass of the halo: after a brief theory overview (Sect. 2), we analyse the trend for both galaxies and galaxy clusters using simulation and real data (Sect. 3), we perform a Bayesian analysis, described in Sect. 4, to establish the slope of the power-law model we assume to describe the IA amplitude signal, and show our results in Sect. 5.

2 THEORETICAL BACKGROUND

The physical picture of tidal interaction of a self-gravitating system that is in virial equilibrium with a velocity dispersion σ, such as an elliptical galaxy or a cluster of galaxies, would be a distortion of the system's gravitational potential through tidal gravitational forces. The particles of the system would remain in virial equilibrium and fill up the distorted potential along an isocontour of the gravitational potential, which would result in a change in the shape of the system. This shape should reflect the magnitude and the orientation of the tidal gravitational fields, and the magnitude of the change in shape should depend on how tightly the system is bound.

In isolated virialised systems the Jeans-equation would apply,

$$\frac{1}{\rho}\frac{\partial}{\partial r}\rho(\sigma^2) + \frac{2}{r}\beta\sigma^2 = -\frac{\partial\Phi}{\partial r}, \tag{1}$$

with the particle density ρ, distance r, gravitational potential Φ and the anisotropy parameter β, which we set to $\beta = 0$ because we aim to derive only the scaling behaviour of the alignment amplitude. In this case, the Jeans-equation can be solved to yield $\rho \propto \exp(-\Phi/\sigma^2)$.

* E-mail: davide.piras@studenti.unipd.it

Gravitational tidal fields generated by the ambient large-scale structure would distort the gravitational potential, and we will work in the limit that the distortion is well-described by a second-order Taylor-expansion relative to the potential minimum,

$$\Phi \rightarrow \Phi + \frac{1}{2}\frac{\partial^2 \Phi}{\partial r_i \partial r_j} r_i r_j \qquad (2)$$

with the distance r_i from the minimum. Consequently, the density of particles would change according to

$$\rho \propto \exp\left(-\frac{\Phi}{\sigma^2}\right) \rightarrow \exp\left(-\frac{\Phi}{\sigma^2}\right)\left(1 + \frac{1}{2\sigma^2}\frac{\partial^2 \Phi}{\partial r_i \partial r_j} r_i r_j\right), \qquad (3)$$

and a measurement of the ellipticity through the second moments of ρ would yield a proportionality to $R^2 \partial^2 \Phi / \sigma^2$, with R the size of the object. The expansion is only valid in the limit of weak tidal fields, which is characterised by $R^2 \partial^2 \Phi / \sigma^2 \ll 1$.

Now, the virial relationship $\sigma^2 = GM/R$ sets the velocity dispersion σ^2 into relation with the gravitational potential $-GM/R$, and with the scaling $M \propto R^3$ one would expect $\sigma^2 \propto M^{2/3}$, such that R^2/σ^2 should be constant. Therefore, any scaling of the ellipticity with mass is entirely due to the dependence of tidal gravitational fields with the mass-scale.

The variance of tidal shear fields can be inferred from the variance of the matter density by the Poisson equation, $\Delta\Phi = 3\Omega_m/(2\chi_H^2)\delta$, with the matter density Ω_m and the Hubble-distance $\chi_H = c/H_0$. Computing the tidal shear fields $\partial^2 \Phi$ shows that they must have the same fluctuation statistics as the density field δ. In Fourier-space, the solution to the Poisson equation is $\Phi \propto \delta/k^2$ with the wave vector k, and the tidal shear fields would become $k_i k_j \Phi \propto k_i k_j/k^2 \delta$. Therefore, the spectrum $P_{\partial^2\Phi}(k)$ of the tidal shear fields is proportional to the spectrum $P_\delta(k)$ of the density fluctuations.

Consequently, one can derive the variance of tidal shear fields from the variance of the density fluctuations, i.e. from the CDM-spectrum $P_\delta(k)$. For doing that, one can relate a mass scale M to the wave vector k by requiring that the mass M should be contained in a sphere of radius R, $M = 4\pi\Omega_m\rho_{crit}R^3/3$, which in turn defines a scale k in the spectrum which is proportional to $M^{-1/3}$. This implies that on galaxy- and cluster-scales, where the CDM-spectrum scales $\propto k^{-2...-3}$, one obtains for the standard deviation of the tidal shear field a behaviour $\propto M^{1/2...1/3}$. We compare these very general theoretical predictions with our results in Sect. 5.

3 DATA

3.1 Simulations

In this work we consider haloes from two different simulations:

(i) the **Millennium Simulation (MS)**, first presented in Springel et al. (2005), which uses 2160^3 dark matter particles of mass $m_P^{MS} = 1.2 \times 10^9 M_\odot$ enclosed in a 500 Mpc/h-side box to sample dark matter haloes and study their growth. In particular, we take into consideration 2 of its 64 snapshots, i.e. the one at $z = 0$ (snapshot 63), which we use for all our analysis, and the one at $z \simeq 0.46$ (snapshot 49), which is studied only as an aside. Dark matter haloes are identified as in Joachimi et al. (2013a) and references therein, assuming that all galaxies share the three-dimensional shape of their host halo. All haloes have a minimum number of particles $N_P = 300$.

(ii) The **Millennium-XXL Simulation (XXL)**, which samples 6720^3 dark matter particles of mass $m_P^{XXL} = 8.456 \times 10^9 M_\odot$ confined in a cubic region of 3000 Mpc/h on a side (Angulo et al. 2012);

in this case, we consider only one snapshot, at $z = 0$. Haloes are selected using an ellipsoidal overdensity algorithm, as described in Despali et al. (2013) and Bonamigo et al. (2015), assuming a minimum number of particles $N_P = 1000$.

In the simulations the same set of cosmological parameters is adopted, namely they both assume a spatially flat ΛCDM universe with the total matter density $\Omega_m = \Omega_b + \Omega_{dm} = 0.25$, where $\Omega_b = 0.045$ indicates baryons and $\Omega_{dm} = 0.205$ represents dark matter, a cosmological constant $\Omega_\Lambda = 1 - \Omega_m = 0.75$, the Hubble parameter $h = 0.73$ and the density variance in spheres of radius 8 Mpc/h $\sigma_8 = 0.9$. All the density parameters are in units of the critical density.

To compare our results with real data, we also take into consideration the analysis presented in van Uitert & Joachimi (2017): in that work, the clusters contained in the redMaPPer catalogue (Rykoff et al. 2014) version 6.3 were used to constrain the intrinsic alignment signal amplitude A_{IA}, which was then studied as a function of the halo mass.

3.2 Halo shapes

We define the simple inertia tensor[1], whose eigenvalues and eigenvectors describe the shape of the halo, as:

$$\mathbf{M}_{\mu\nu} \propto \sum_{i=1}^{N_P} r_{i,\mu} r_{i,\nu}, \qquad (4)$$

where N_P is the total number of particles within the halo, and $\mathbf{r}_i$ is the vector that indicates the position of the i-th particle with respect to the centre of the halo, i.e. the location of the gravitational potential minimum. For the MS only, we also consider a reduced inertia tensor, which is defined as (Pereira et al. 2008):

$$\mathbf{M}_{\mu\nu}^{red} \propto \sum_{i=1}^{N_P} \frac{r_{i,\mu} r_{i,\nu}}{r_i^2}, \qquad (5)$$

with r_i^2 the square of the three-dimensional distance of the i-th particle from the centre of the halo; the reduced inertia tensor is more weighted towards the centre of the halo, and may yield a more reliable approximation of the shape of the galaxy (Joachimi et al. 2013b; Chisari et al. 2015).

The eigenvectors define an ellipsoid, which we project onto one of the faces of the cube that hosts the simulation: the resulting ellipse is the shape of the galaxy, which is assumed to be the same as the shape of the host halo. We proceed as in Joachimi et al. (2013a,b) to define the ellipticity ϵ of the galaxy, considering our objects as early-type galaxies: indicating the three unit eigenvectors as $\mathbf{s}_\mu = \{s_{x,\mu}, s_{y,\mu}, s_{\parallel,\mu}\}^\mathsf{T}$ and the absolute values of the semi-axes as ω_μ, $\mu \in \{1, 2, 3\}$, we define a symmetric tensor

$$\mathbf{W}^{-1} = \sum_{\mu=1}^{3} \frac{s_{\perp,\mu} s_{\perp,\mu}^\mathsf{T}}{\omega_\mu^2} - \frac{\kappa\kappa^\mathsf{T}}{\alpha^2}, \qquad (6)$$

with $s_{\perp,\mu} = \{s_{x,\mu}, s_{y,\mu}\}^\mathsf{T}$ the eigenvector projected along the line of sight,

$$\kappa = \sum_{\mu=1}^{3} \frac{s_{\parallel,\mu} \mathbf{s}_{\perp,\mu}}{\omega_\mu^2}, \qquad (7)$$

---

[1] MS and XXL use two different tensors to describe the shape, but our choice has no impact on the ellipticity of the haloes (see also Bett et al. (2007) for further details).

and

$$\alpha^2 = \sum_{\mu=1}^{3} \left(\frac{s_{\parallel,\mu}}{\omega_\mu} \right)^2 . \tag{8}$$

We then compute the two components of the ellipticity (Bartelmann & Schneider 2001):

$$\epsilon_1 = \frac{W_{11} - W_{22}}{W_{11} + W_{22} + 2\sqrt{\det \mathbf{W}}} \; ; \tag{9}$$

$$\epsilon_2 = \frac{2W_{12}}{W_{11} + W_{22} + 2\sqrt{\det \mathbf{W}}} \; . \tag{10}$$

4 METHODOLOGY

4.1 Measurements

To measure the correlation between the shapes of galaxy clusters and the density field we define an estimator as a function of the comoving transverse distance R_p and the line-of-sight distance Π:

$$\hat{\xi}_{g+}(R_p, \Pi) = \frac{S_+ D}{DD} , \tag{11}$$

where $S_+ D$ represents the correlation between cluster shapes and the density sample and DD the number of cluster shape - density pairs. We then integrate along the line of sight to obtain the total projected intrinsic alignment signal:

$$\hat{w}_{g+}(R_p) = \int_{-\Pi_{max}}^{\Pi_{max}} d\Pi \, \hat{\xi}_{g+}(R_p, \Pi) . \tag{12}$$

Throughout this work, we adopt $\Pi_{max} = 60$ Mpc/h, a value large enough not to miss part of the signal, but small enough not to pick up too much noise. We describe the intrinsic alignment signal by simplifying the model in van Uitert & Joachimi (2017, equation 5), namely we assume:

$$w_{g+}(R_p, M) = A_{IA}(M) \, b_g(M) \, w_{\delta+}^{model}(R_{pp}) , \tag{13}$$

with $A_{IA}(M)$ the amplitude of the intrinsic alignment signal, $b_g(M)$ the cluster bias and $w_{\delta+}^{model}(R_p)$ a function in which we include the dependence on R_p; the dependence on the mass of the halo M is in both the $A_{IA}(M)$ and $b_g(M)$ factors. We evaluate the expression in Eq. 13 in the interval which covers 6 Mpc/h < R_p < 30 Mpc/h, denoted by R_p^*, to get rid of the dependence on R_p; in other words, we define:

$$w_{g+}(M) = w_{g+}(R_p = R_p^*, M) . \tag{14}$$

We use the LS (Landy & Szalay 1993) estimator to calculate the clustering signal:

$$\hat{\xi}_{gg}(R_p, \Pi) = \frac{DD - 2DR + RR}{RR} , \tag{15}$$

where DD represents the number of cluster pairs, DR the number of cluster - random point pairs, and RR the number of random point pairs. We then integrate along the line of sight to obtain the total projected clustering signal:

$$\hat{w}_{gg}(R_p) = \int_{-\Pi_{max}}^{\Pi_{max}} d\Pi \, \hat{\xi}_{gg}(R_p, \Pi) . \tag{16}$$

We describe the clustering signal with a simple model:

$$w_{gg}(R_p, M) = b_g^2(M) \, w_{\delta\delta}^{model}(R_p) - C_{IC} , \tag{17}$$

with $w_{\delta\delta}^{model}(R_p)$ a function in which we include the dependence on

R_p (van Uitert & Joachimi 2017, equation 9), and C_{IC} the integral constraint factor, which we estimate as in Roche & Eales (1999, equation 8) using the random pair counts. Again, we evaluate the previous expression in R_p^*, obtaining:

$$w_{gg}(M) = w_{gg}(R_p = R_p^*, M) . \tag{18}$$

To get rid of the cluster bias $b_g(M)$ factor and focus on the mass dependence of the amplitude $A_{IA}(M)$, we define:

$$r_{g+}(M) = \frac{w_{g+}(M)}{\sqrt{w_{gg}(M)}} = \frac{A_{IA}(M) w_{\delta+}^{model}(R_p = R_p^*)}{\sqrt{w_{\delta\delta}^{model}(R_p = R_p^*)}} \propto A_{IA}(M) , \tag{19}$$

where we assume that the clustering signal $w_{gg}(M)$ is positive (see Sect. 4.2 and Sect. 5 for further discussion). We stress that this quantity depends only on the mass of the halo M.

4.2 Modelling

The goal of this paper is to study the dependence on the mass of the amplitude $A_{IA}(M)$ by studying the quantity $r_{g+}(M)$: assuming that

$$A_{IA}(M) \propto M^\beta , \tag{20}$$

we adopt the following model for $r_{g+}(M)$:

$$r_{g+}(M) = A \cdot \left(\frac{M}{M_p} \right)^\beta , \tag{21}$$

with A a generic amplitude with no physical meaning, $M_p = 10^{13.5} M_\odot/h_{70}$ a pivot mass and β as in Eq. 20.

To achieve this goal, we select the objects of the catalogues described in Sect. 3.1 in $n = 4$ logarithmic mass bins, between $10^{11.5} M_\odot$ and $10^{14} M_\odot$ for the MS and between $10^{13} M_\odot/h$ and $10^{15} M_\odot/h$ for the XXL, we split them in $N = 3^3 = 27$ sub-boxes based on their positions inside the cube of the respective simulation, and calculate w_{g+} and w_{gg} for each of the N sub-samples by replacing the integrals in Eq. 12 and 16 with a sum over 20 line-of-sight bins, each $(\Pi_{max} - (-\Pi_{max}))/20 = 6$ Mpc/h wide. We define the mass of these objects as the mass within a halo which has mean density 200 times the critical value at the redshift corresponding to the respective snapshot (M_{200c}); note that for the MS we first convert the halo mass from M_{Dhalo}, as defined in Jiang et al. (2014), to M_{200c} using the median line in Jiang et al. (2014, figure 2). We show the distribution of the selected masses for the two catalogues in Fig. 1.

To measure DR and RR as in Eq. 15, we generate random catalogues that contain objects uniformly distributed between the minimum and maximum value of the x, y and z coordinates of each sub-box. These catalogues normally are 3 times denser; in some cases, when a sub-box encloses very few objects, we switch to random catalogues which are 10 times denser.

We then perform a posterior analysis over the data to retrieve the distributions of A and β: according to Bayes' theorem, if $\boldsymbol{d}$ is the vector of the data and $\boldsymbol{p}$ the vector of the parameters,

$$P(\boldsymbol{p}|\boldsymbol{d}) \propto P(\boldsymbol{d}|\boldsymbol{p}) \, P(\boldsymbol{p}) \propto e^{-\frac{1}{2}\chi^2} P(\boldsymbol{p}) , \tag{22}$$

with $P(\boldsymbol{p}|\boldsymbol{d})$ the posterior probability, $P(\boldsymbol{d}|\boldsymbol{p})$ the likelihood function, $P(\boldsymbol{p})$ the prior probability and $\chi^2 = (\boldsymbol{d}-\boldsymbol{m})^T \mathbf{C}^{-1}(\boldsymbol{d}-\boldsymbol{m})$, with $\boldsymbol{m}$ the vector of the model and $\mathbf{C}^{-1}$ the precision matrix, the inverse of the covariance matrix $\mathbf{C}$. We assume uninformative flat priors in the fit with ranges $\log_{10} A \in [-2.3; -0.4]$ and $\beta \in [-0.50; 0.75]$.
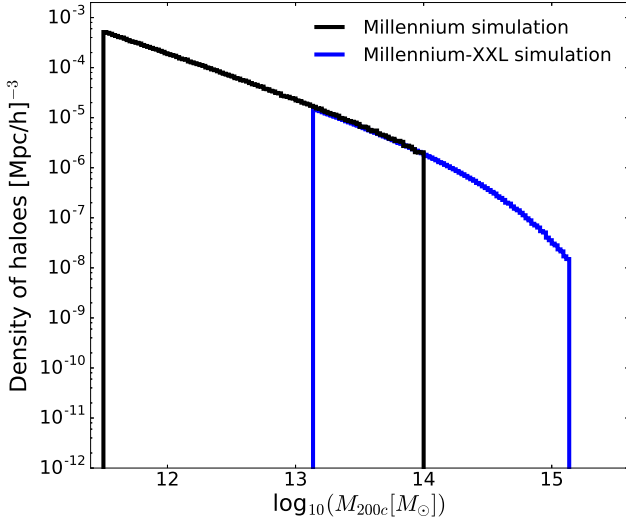
Figure 1. Histogram showing the density distribution of the mass of the haloes. In this case, the mass of the halo is defined considering an overdensity of 200 times the critical value (M_{200c}).

We estimate the covariance matrix from the data as in Taylor et al. (2013):

$$\mathbf{C}_{\mu\nu} = \frac{1}{N-1} \sum_{j=1}^{N} (x_{j,\mu} - \overline{x}_{\mu})(x_{j,\nu} - \overline{x}_{\nu}),\qquad(23)$$

with $\mu, \nu \in \{1, \ldots, n\}$, $\overline{x}_{\mu} = \frac{1}{N} \sum_{j=1}^{N} x_{j,\mu}$, and $x_{j,\mu} = r_{g+}(M)$ for each sub-box and each mass bin, as defined in Eq. 19. We then invert the covariance matrix and correct the bias on the inverse to obtain an unbiased estimate of the precision matrix, given by:

$$\mathbf{C}_{\text{unbiased}}^{-1} = \frac{N-n-2}{N-1}\,\mathbf{C}^{-1},\qquad(24)$$

where $N > n + 2$ clearly holds (Taylor et al. 2013). The results of the analysis are presented in Sect. 5.

The choice of n and N is constrained by many factors: first of all, if N is too large the single values of w_{gg} (and w_{g+}) tend to fluctuate around the mean, thus increasing the error bar and sometimes plunging below 0, which is obviously unacceptable for our choice of $r_{g+}(M)$ (see Eq. 19). Furthermore, we want n to be large enough to be capable of displaying the trend of the signals along the whole mass range chosen. Finally, we need to take $n \ll N$ to avoid divergences related to the fact that we estimate the covariance from a finite number of samples (Taylor et al. 2013).

5 RESULTS AND DISCUSSION

The trend of w_{g+} and w_{gg} with R_p for the lowest, middle and highest mass bin for both the catalogues is shown in Fig. 2; note that even though in the chosen interval w_{gg} is not always positive within the error bar, our choice of n and N ensures that Eq. 19 always returns a real value. The points showed in Fig. 2 are the arithmetical mean of the N values for each mass bin, while the error bars are represented by the standard deviation of the values. The overall behaviour of w_{g+} and w_{gg} agrees with previous works (Joachimi et al. 2011; van Uitert & Joachimi 2017) and the upper plot in each panel suggests the detection of a positive alignment, meaning that clusters point
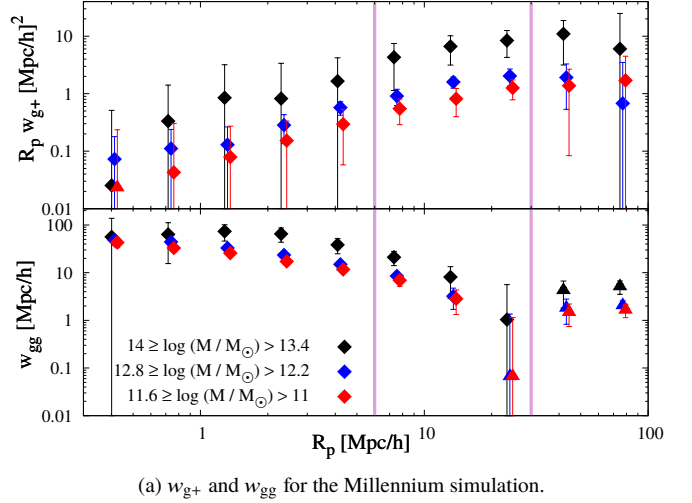
(a) w_{g+} and w_{gg} for the Millennium simulation.
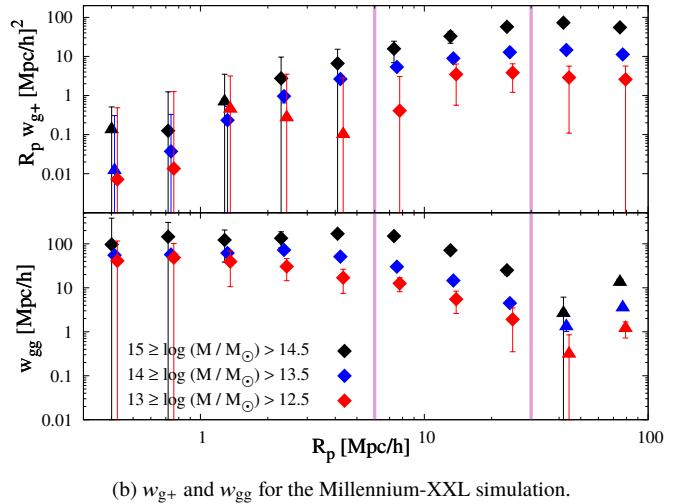
(b) w_{g+} and w_{gg} for the Millennium-XXL simulation.

Figure 2. Trend of the intrinsic alignment signal w_{g+} and the cluster signal w_{gg} with the comoving transverse distance R_p for (a) the Millennium and (b) the Millennium-XXL simulation. The pink lines indicate the $6 < R_p/\text{Mpc}/h < 30$ interval. Black, blue and red dots represent respectively the highest, middle and lowest mass bin of each catalogue; negative values are displayed in absolute value with different symbols of the same colour. In the graph, points are slightly shifted, so that they do not overlap.

towards nearby clusters; also, it is worth noting that both signals increase with increasing mass.

We then study the dependence of w_{g+}, w_{gg} and r_{g+} on the mass of the halo. To be able to compare our results with those in van Uitert & Joachimi (2017, figure 7) we convert our M_{200c} to M_{200m}, defined as the mass within a halo which has mean density 200 times the mean background value at the redshift corresponding to the respective snapshot. In Fig. 3 we also include, for the Millennium simulation only, two more results: grey dots represent the signal from the objects at redshift $z = 0.46$, while open black dots represent the signal from the objects at $z = 0$ obtained using the reduced inertia tensor (*rit*), instead of the simple one, to measure the shapes of the haloes. As one can see, despite the use of two different quantities to measure the shapes, as mentioned in Sect. 3.2, the MS and the XXL yield consistent results in the mass range where they overlap; furthermore, all three w_{g+}, w_{gg} and r_{g+} increase with increasing mass. As a side note, we mention that the *rit* leads to lower alignment
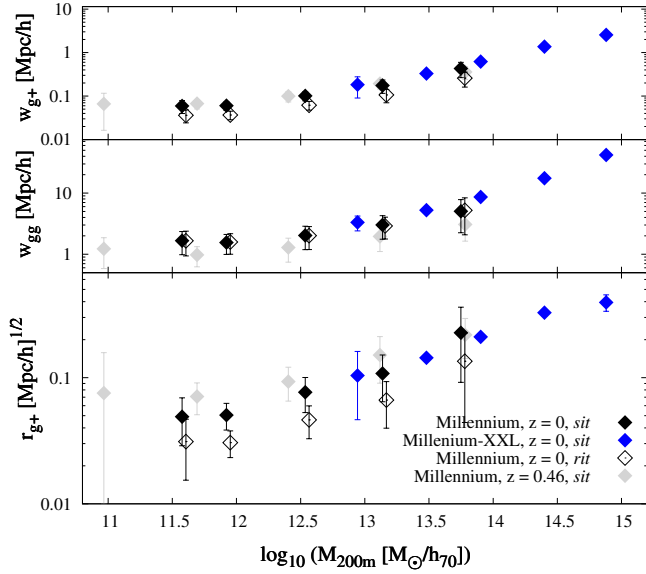
Figure 3. Trend of the intrinsic alignment signal w_{g+}, the cluster signal w_{gg} and r_{g+} as defined in Eq. 19 with the halo mass M_{200m} for the Millennium and the Millennium-XXL simulations. The label *sit* stands for simple inertia tensor, while *rit* means reduced inertia tensor; note that for the XXL data only the simple inertia tensor is available, as mentioned in Sect. 3.2. The grey dots cover a different mass range, namely (TBD) due to high noise at the high-mass end of the interval; moreover, these points reach very low mass values, where the choice of the threshold $N_p = 300$ could lead to spurious alignments. The points are not placed at the midpoint of the bin, but at the value corresponding to the arithmetic mean of the mass of the objects. Points showing the results from the *rit* choice are artificially shifted, so that they do not overlap with the corresponding *sit* dots.

signals, as found in Joachimi et al. (2013b), and that, on the other hand, these signals increase with increasing redshift.

We proceed by showing the results of the posterior analysis described in Sect. 4.2: Fig. 4(a) shows the results from the single catalogues and from the joint analysis of the two simulations, obtained by multiplying the likelihood functions and assuming the same flat priors on the parameters. The most stringent bounds come from the MXXL simulation, while the Millennium yields larger errors on the parameters, even though consistent with the results of the XXL. It is worth noting that the joint analysis leads to a slope compatible with $\beta = 1/3$, which agrees with the predictions made in Sect. 2 for a CDM-only Universe.

We perform a posterior analysis also on the real data. In van Uitert & Joachimi (2017, figure 7) the results of their study are shown together with results from previous papers (Joachimi et al. 2011; Singh et al. 2015): we consider all the 21 points in the plot, neglect the error bars on the mass and treat all the data as independent, so that the covariance matrix is diagonal. We show the points, together with the best-fit line from our analysis, in Fig. 5.

In this case, we need to slightly change the model in Eq. 21, since we are dealing with a different quantity. We assume:

$$A_{IA}(M) = A_r \cdot \left(\frac{M}{M_p}\right)^\beta , \tag{25}$$

where the prefactor A_r is now dimensionless, thus making it impossible to directly compare its value to the one that is suggested by the simulation data. We also assume different flat priors in the fit for the parameters, namely $\log_{10} A_r \in [0.4; 0.9]$ and $\beta \in [0.4; 0.7]$. The outcomes of our analysis are shown in Fig. 4 and in Table 1:

we observe that the value of the reduced chi-square for this latter analysis is not as good as in the analysis with the simulated data, but can be improved to 1.36 by excluding the high-redshift SDSS results (filled-blue diamonds) without affecting the value of the slope in a significant way.

We note that while the disagreement between the values of the prefactor can be easily justified, since we are using different definitions of the amplitude of the intrinsic alignment signal, the incompatibility between the values of the slope β is not straightforward, and could be explained by more profound factors. To begin with[2], the simulations presented in this work consider a CDM-only Universe, neglecting the influence of gas and dust: a possible future work in this sense would be to test the slope β using a hydrodynamical simulation, which could then account for these additional effects.

6 CONCLUSIONS

The last numbered section should briefly summarise what has been done, and describe the final conclusions which the authors draw from their work.

REFERENCES

Angulo R. E., Springel V., White S. D. M., Jenkins A., Baugh C. M., Frenk C. S., 2012, MNRAS, 426, 2046
Bartelmann M., Schneider P., 2001, Phys. Rep., 340, 291
Bett P., Eke V., Frenk C. S., Jenkins A., Helly J., Navarro J., 2007, MNRAS, 376, 215
Bonamigo M., Despali G., Limousin M., Angulo R., Giocoli C., Soucail G., 2015, MNRAS, 449, 3171
Chisari N., et al., 2015, MNRAS, 454, 2736
Codis S., et al., 2015, MNRAS, 448, 3391
Croft R. A. C., Metzler C. A., 2000, ApJ, 545, 561
Despali G., Tormen G., Sheth R. K., 2013, MNRAS, 431, 1143
Hao J., Kubo J. M., Feldmann R., Annis J., Johnston D. E., Lin H., McKay T. A., 2011, ApJ, 740, 39
Heavens A., Refregier A., Heymans C., 2000, MNRAS, 319, 649
Heymans C., White M., Heavens A., Vale C., Van Waerbeke L., 2006, MNRAS, 371, 750
Hilbert S., Xu D., Schneider P., Springel V., Vogelsberger M., Hernquist L., 2017, MNRAS, 468, 790
Hirata C. M., Mandelbaum R., Ishak M., Seljak U., Nichol R., Pimbblet K. A., Ross N. P., Wake D., 2007, MNRAS, 381, 1197
Jiang L., Helly J. C., Cole S., Frenk C. S., 2014, MNRAS, 440, 2115
Jing Y. P., 2002, MNRAS, 335, L89
Joachimi B., Mandelbaum R., Abdalla F. B., Bridle S. L., 2011, A&A, 527, A26
Joachimi B., Semboloni E., Bett P. E., Hartlap J., Hilbert S., Hoekstra H., Schneider P., Schrabback T., 2013a, MNRAS, 431, 477
Joachimi B., Semboloni E., Hilbert S., Bett P. E., Hartlap J., Hoekstra H., Schneider P., 2013b, MNRAS, 436, 819
Joachimi B., et al., 2015, Space Sci. Rev., 193, 1
Kiessling A., et al., 2015, Space Sci. Rev., 193, 67
Kuhlen M., Diemand J., Madau P., 2007, ApJ, 671, 1135
LSST Science Collaboration et al., 2009, preprint, (arXiv:0912.0201)
Landy S. D., Szalay A. S., 1993, ApJ, 412, 64
Laureijs R., et al., 2011, preprint, (arXiv:1110.3193)

---

[2] Include reasons for discrepancy - to be completed.

(a) Single and joint posterior analysis for the simulations.

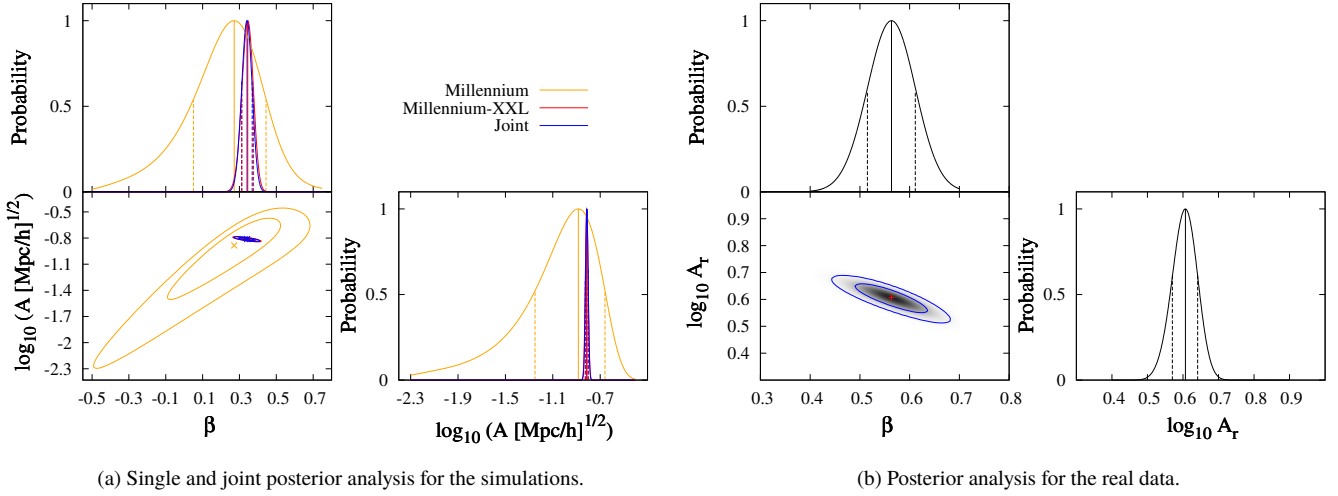(b) Posterior analysis for the real data.

Figure 4. Posterior analysis for (a) the Millennium simulation, the MXXL simulation, joint MS and XXL, and (b) real data; note that the ranges of the parameters are quite different. The bottom-left graph in the left panel shows the contour lines for all the simulations (single and joint), but the 2-D posterior for the joint analysis only; the bottom-left graph in the right panel shows the 2-D posterior for the real data. All other sub-panels show the marginalized 1-D posterior normalized to a peak amplitude of 1. Contour lines enclose the 68% and 95% confidence intervals, dots and vertical solid lines indicate the best-fitting values while dashed lines represent the 1-σ confidence interval. We note that the MS returns larger error bars, but the results are consistent for the two catalogues, while real data yield a value of the slope which is incompatible with the one from the joint analysis. The exact values and errors of A, A_r and β are presented in Table 1.

Table 1. Results of the posterior analysis over the Millennium simulation, the Millennium-XXL simulation, their joint contribution, the Milennium simulation at $z = 0.46$, the Millennium simulation using the *rit* and real data. Note that the values from the snapshot at different redshift and from the reduced inertia tensor assumption are compatible with the outcomes of the MS only analysis; these results are not shown in Fig. 4(a), though.

	MS only	XXL only	Joint	MS, $z = 0.46$	MS, *rit*
β	$0.27^{+0.17}_{-0.22}$	$0.35^{+0.03}_{-0.03}$	$0.34^{+0.03}_{-0.03}$	$0.23^{+0.10}_{-0.12}$	$0.28^{+0.16}_{-0.20}$
$\log_{10}(A\,[\mathrm{Mpc}/h]^{1/2})$	$-0.88^{+0.23}_{-0.37}$	$-0.81^{+0.01}_{-0.01}$	$-0.81^{+0.01}_{-0.01}$	$-0.78^{+0.15}_{-0.24}$	$-1.09^{+0.21}_{-0.33}$
χ^2/dof	0.14	0.91	0.42	0.08	0.12

	Real data
β	$0.56^{+0.05}_{-0.05}$
$\log_{10} A_r$	$0.61^{+0.03}_{-0.04}$
χ^2/dof	1.68

Mandelbaum R., Hirata C. M., Ishak M., Seljak U., Brinkmann J., 2006, MNRAS, 367, 611
Mandelbaum R., et al., 2011, MNRAS, 410, 844
Okumura T., Jing Y. P., Li C., 2009, ApJ, 694, 214
Pereira M. J., Bryan G. L., Gill S. P. D., 2008, ApJ, 672, 825
Roche N., Eales S. A., 1999, MNRAS, 307, 703
Rykoff E. S., et al., 2014, ApJ, 785, 104
Schneider M. D., Frenk C. S., Cole S., 2012, J. Cosmology Astropart. Phys., 5, 030
Semboloni E., Heymans C., van Waerbeke L., Schneider P., 2008, MNRAS, 388, 991
Singh S., Mandelbaum R., More S., 2015, MNRAS, 450, 2195
Springel V., et al., 2005, Nature, 435, 629
Taylor A., Joachimi B., Kitching T., 2013, MNRAS, 432, 1928
Tenneti A., Mandelbaum R., Di Matteo T., 2016, MNRAS, 462, 2668
Troxel M. A., Ishak M., 2015, Phys. Rep., 558, 1
Velliscig M., et al., 2015, MNRAS, 454, 3328
van Uitert E., Joachimi B., 2017, preprint, (arXiv:1701.02307)

This paper has been typeset from a TEX/LATEX file prepared by the author.

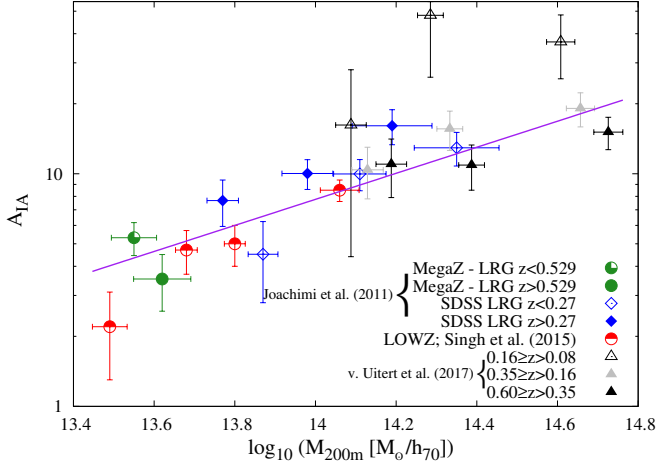**Figure 5.** Real data, as shown in van Uitert & Joachimi (2017, figure 7), with the best-fit line from our posterior analysis. The exact values of the parameters are shown in Table 1.